

# Physics of bioprinting


Cite as: Appl. Phys. Rev. **6**, 021315 (2019); <https://doi.org/10.1063/1.5087206>

Submitted: 29 December 2018 • Accepted: 23 April 2019 • Published Online: 04 June 2019

 Ashkan Shafiee,  Elham Ghadiri,  Haripriya Ramesh, et al.

## COLLECTIONS

Paper published as part of the special topic on [3D Bioprinting: Physical and Chemical Processes](#)

 This paper was selected as Featured



View Online



Export Citation



CrossMark

## ARTICLES YOU MAY BE INTERESTED IN

[Extrusion bioprinting of soft materials: An emerging technique for biological model fabrication](#)  
Applied Physics Reviews **6**, 011310 (2019); <https://doi.org/10.1063/1.5059393>

[Resolution and shape in bioprinting: Strategizing towards complex tissue and organ printing](#)  
Applied Physics Reviews **6**, 011307 (2019); <https://doi.org/10.1063/1.5053909>

[Tissue-engineering of vascular grafts containing endothelium and smooth-muscle using triple-coaxial cell printing](#)  
Applied Physics Reviews **6**, 041402 (2019); <https://doi.org/10.1063/1.5099306>



# Physics of bioprinting

Cite as: Appl. Phys. Rev. **6**, 021315 (2019); doi: [10.1063/1.5087206](https://doi.org/10.1063/1.5087206)

Submitted: 29 December 2018 · Accepted: 23 April 2019 ·

Published Online: 4 June 2019










View Online



Export Citation



CrossMark

Ashkan Shafiee,<sup>1,a)</sup>  Elham Ghadiri,<sup>1,2</sup>  Haripriya Ramesh,<sup>3</sup>  Carlos Kengla,<sup>1</sup>  Jareer Kassis,<sup>1</sup> Paul Calvert,<sup>4</sup> David Williams,<sup>1</sup>  Ali Khademhosseini,<sup>5</sup>  Roger Narayan,<sup>3</sup>  Gabor Forgacs,<sup>6,7</sup> and Anthony Atala<sup>1</sup>

## AFFILIATIONS

<sup>1</sup>Wake Forest Institute for Regenerative Medicine, Wake Forest School of Medicine, Winston-Salem, North Carolina 27157, USA

<sup>2</sup>Department of Chemistry, Wake Forest University, Winston-Salem, North Carolina 27109, USA

<sup>3</sup>UNC/NCSSU Joint Department of Biomedical Engineering, Raleigh, North Carolina 27695, USA

<sup>4</sup>Department of Chemical Engineering, New Mexico Tech, Socorro, New Mexico 87801, USA

<sup>5</sup>Department of Bioengineering, Department of Radiology, Department of Chemical and Biomolecular Engineering, Center for Minimally Invasive Therapeutics, Jonsson Comprehensive Cancer Center, University of California, Los Angeles, California 90095, USA

<sup>6</sup>Department of Physics, University of Missouri, Columbia, Missouri 65211, USA

<sup>7</sup>Modern Meadow, Inc., Nutley, New Jersey 07110, USA

**Note:** This paper is part of the Special Topic on 3D Bioprinting: Physical and Chemical Processes.

<sup>a)</sup>Author to whom correspondence should be addressed: [ashafiee@wakehealth.edu](mailto:ashafiee@wakehealth.edu)

## ABSTRACT

Bioprinters are being extensively used for different applications in life sciences and medicine in general and more specifically in regenerative medicine, tissue, and organ fabrication. The technology has matured from its purely academic origin owing to the involvement of materials science, engineering, biology, and physics, as well as commercial entities. Nevertheless, despite the progress in the science and the understanding of the mechanisms underlying the various bioprinting technologies, further efforts are needed to develop more quantitative strategies. In particular, predictive modeling is necessary to optimize the printing parameters and thus enhance the quality of the final products. Here, we review the physics that underpins the most commonly employed approaches, such as extrusion, laser-based, and inkjet bioprinting. We provide an overview of the relevant parameters, their inter-relationships, and the equations that govern the various printing processes and thus allow for their optimization. We present our perspective on the field and views on future strategies for its further advancement. Our intention with this review is to provide the practitioners of bioprinting with additional tools to enhance the quantitative aspects of their work and move the technology beyond its early, mostly “trial and error” character.

Published under license by AIP Publishing. <https://doi.org/10.1063/1.5087206>

## TABLE OF CONTENTS

INTRODUCTION.....	1	Newtonian and non-newtonian fluid dynamics.....	6
PHYSICS OF EXTRUSION BIOPRINTING.....	2	Pneumatic extrusion.....	8
Physics of tissue extrusion bioprinting.....	2	Mechanical extrusion.....	8
Differential adhesion hypothesis and tissue liquidity.....	3	PHYSICS OF INKJET PRINTING.....	8
Apparent tissue surface tension.....	3	Fluid properties for bioink printability.....	8
Cell sorting.....	4	PHYSICS OF LASER ASSISTED BIOPRINTING.....	9
Physics of cell sorting.....	4	CONCLUSIONS.....	12
Tissue fusion.....	4		
Physics of tissue fusion.....	4		
TISSUE MATURATION ACCELERATION.....	5		
TISSUE MATURATION MODELING.....	6		
Cellular particle dynamics.....	6		
PHYSICS OF EXTRUSION BIOPRINTING.....	6		

## INTRODUCTION

Printing technologies have become useful for a wide range of applications in medicine and human healthcare. The unique advantages of bioprinting, such as computer-aided fabrication, speed, and accuracy of delivering different materials, have increased the technique's popularity.<sup>1</sup> Bioprinters are being used extensively in applications

such as biosensing,<sup>2–4</sup> drug delivery,<sup>5</sup> tissue engineering,<sup>6</sup> oncology,<sup>7–9</sup> surgical planning,<sup>10–13</sup> and regenerative medicine.<sup>14</sup> Meanwhile, more advanced printer types and printing materials continue to be developed.

Extrusion,<sup>6,15</sup> inkjet,<sup>16</sup> and laser-based bioprinters<sup>17,18</sup> are the most popular currently employed. Extrusion bioprinters can dispense viscous materials using mechanical or pneumatic forces; the bioink is loaded into a syringe or special reservoir and is then printed using a piston or air pressure with controlled speed. (In this article, bioink simply refers to the material delivered by the bioprinter. Thus, it may designate purely a cellular material, cell-laden hydrogel, or innate polymer to be used to print a scaffold. For the distinction between cells containing bioink and biomaterial ink, see Refs. 27 and 28.) This printing technique incorporates tissue extrusion (i.e., printing of purely cellular materials), mostly used in scaffold-free tissue engineering, cell-free biomaterial printing (i.e., various hydrogels, such as gelatin, alginate, and collagen) for scaffold-based tissue engineering and everything in between (i.e., cell-laden hydrogels). Purely cellular bioinks composed of a mixture of different cell types can be printed in spherical or cylindrical shapes to create multicellular systems and/or microtissues. The final bioprinted product is obtained when the deposited bioink units undergo self-assembly (e.g., through cell sorting and fusion). Inkjet bioprinters can be used for less viscous materials; these printers use either a piezoelectric crystal or heater that is attached to the ink reservoir to create droplets that are a few picoliters in size. Laser bioprinters use a laser beam that is focused on a ribbon composed of an absorbing material.

The specific type of printer used in an application depends on the nature of the desired bioprinted product.<sup>19</sup> Extrusion printers have been shown to provide the best results for printing tissues, multicellular systems, cell-laden biomaterials, and other high-viscosity materials for the fabrication of three-dimensional (3D) structures.<sup>6,20</sup> Inkjet printers have shown high efficiency in the use of materials and patterning of cells and materials with low viscosity and surface tension.<sup>16,21–23</sup> Laser-based bioprinters, being orifice-less systems, have excellent resolutions for printing functional materials and cellular structures without the nozzle clogging problem.<sup>17,24,25</sup> In inkjet printing and extrusion, however, by reducing the size of the orifice to increase the resolution, we may increase the chance of nozzle clogging.

As the field is expanding, there is an increasing need for the printing of new materials that have more sophisticated properties and geometries. However, the science behind this technology is underappreciated and underused despite extensive global efforts to advance bioprinting technology. Unlike the 3D printing of inert materials that can be used for the manufacturing of typical non-biologically active objects, biological products are not ready immediately after bioprinting.<sup>26</sup> Post-bioprinting processes are essential before the biological constructs are ready for use. In addition, the critical parameters devised prior to and during the printing process must be optimized for consistent manufacturing of a reliable final product. Such optimization necessitates a detailed understanding of the underlying physical characteristics behind the printing procedure, including imperative parameters, relationships, and governing equations.

The objective of this review is to present a scientific and conceptual overview of the field of bioprinting. Specifically, we discuss the three most popular bioprinting methods, extrusion, inkjet, and laser-based bioprinters and provide an insight into the science underlying

these printing technologies. We categorize these printing methods based on their physics underpinning and comprehensively overview the respective relevant parameters and their inter-relationship. We hope to accomplish this in a manner that is informative for both beginners and experts. Each section of this review is designed to help researchers using a particular printer type find useful information on the underlying physical concepts independent of other sections.

## PHYSICS OF EXTRUSION BIOPRINTING

### Physics of tissue extrusion bioprinting

The underlying physics of extrusion tissue printing is perhaps the most developed of all bioprinting types. Tissue printing is a scaffold-free tissue engineering method that applies the principles of biological physics that governs embryonic development.<sup>19,29</sup> Many steps of morphogenesis that are based on physical phenomena have been used in bioprinting. Bioprinting of microtissues/multicellular systems provides cells with the appropriate conditions to self-assemble into functional structures, such as tissues and eventually organs. The physics of biological structure formation provides reliable tools to design experiments using bioprinting and to predict the outcome of printing. This includes but is not limited to the mechanisms by which tissues and organs form and self-assemble in the developing embryo.<sup>30–32</sup> Self-assembly and the maturation of the printed structure occur post-bioprinting in bioreactors through the fusion of the bioinks and the reorganization of the cells within them.

Embryonic development is a highly orchestrated sequence of events that is based on the complex interplay of genetic and molecular processes on one hand and biochemical and physical mechanisms on the other.<sup>33</sup> As the embryo progresses from the initial, single-cell zygote to the multicellular stage with many specialized differentiated cells and finally the multi-organ complex, it utilizes numerous morphogenetic self-assembly principles. Understanding these processes is a prerequisite for their application in self-assembly based bioprinting of microtissues.<sup>33,34</sup> In this approach, only the cellular material is used for the bioinks, and cells are provided with initial conditions consistent with the desired tissue or organ structure and cellular self-assembly into the final product (in the course of which, among other events, they secrete their own extracellular matrix).

In particular, the conditions imply the printing of cells into an initial configuration that is compatible with the shape of the intended biological structure.<sup>15,35,36</sup> Bioink particles that comprise cell aggregates of certain compositions are delivered into a supporting material using sophisticated templates based on the topology of the desired biological structure.<sup>35</sup> Biological structures form in the course of post-printing maturation by the fusion of the bioinks and the sorting of cells within them, both fusion and sorting representing fundamental morphogenetic processes.<sup>37</sup> The distinguishing feature of this bioprinting approach, compared to other methods, is that the bioinks themselves are 3D tissue fragments. Consequently, cells are in a more physiologically relevant arrangement as they are in adhesive contact with their surrounding cells, assuring the transmission of important molecular signals. Extrusion bioprinting produces higher-density biological structures compared to other bioprinting technologies and thus is the most suitable for tissue fabrication.

In tissue extrusion bioprinting, the bioink is a multicellular aggregate, essentially a mini-tissue.<sup>1,20,38</sup> Different cell types can be printed individually or collectively (a mixture of multiple cells). The printed

cellular systems (bioinks) self-assemble and allow the maturation of the post-printed structure into an implantable product. As post-bioprinting maturation (the main difference between 3D bioprinting and ordinary 3D printing) is a time-dependent process, it can be argued that bioprinting encompasses the fourth dimension: time. The fact that the bioink is a cell-based system implies that the physics governing extrusion tissue bioprinting is similar to that evident in the behavior of multicellular systems.

### Differential adhesion hypothesis and tissue liquidity

One of the most important processes underlying the transformation of the single-cell zygote into a multicellular organism is cell adhesion.<sup>39</sup> Tissue printing is heavily reliant on early developmental mechanisms related to adhesion, such as cell sorting and tissue fusion.<sup>40</sup>

The “differential adhesion hypothesis” (DAH) was formulated by Steinberg in 1963; it postulates that different cell types manifest different strengths of adhesion as one of their inherent properties.<sup>41</sup> It was shown that embryonic tissue segregation and the rearrangement of mobile cells are dominated by differences in intercellular adhesion.<sup>41</sup> Furthermore, an analogy was offered between unmixable liquids (e.g., water and oil) and multicellular systems in mutual contact. This analogy has been interpreted in terms of the DAH.<sup>33,35,42</sup> This indicates that using the minimization of interfacial and surface free energies, an initial amalgam of various cell types is driven to reach a “phase-separated” arrangement that can be characterized by apparent tissue surface tension (ATST;  $\gamma$ ).<sup>33</sup> The word “apparent” signifies that ATST is not identical to fluid surface tension but rather a convenient and effective parameter. In particular, the concept of ATST allows the prediction of the shape and composition of the phase-separated multicellular assembly (e.g., in a spheroid in which one of the two cell types surrounds the other). ATST has been extensively used to interpret a number of critical processes in embryonic development<sup>43</sup> and to investigate the *in vitro* invasion pattern of tumors.<sup>44,45</sup> It has now been demonstrated to also play an important role in bioprinting.<sup>26</sup> DAH and its predictions have been observed and verified in many

experiments, and the ATST has been measured in several studies.<sup>26,41,46–50</sup> A correlation has been shown between ATST and the strength of adhesion in aggregates; the DAH predicts that cells with stronger adhesions exhibit higher ATST. This prediction has been confirmed in many *in vitro* investigations.<sup>49,51–53</sup>

### Apparent tissue surface tension

ATST is the macroscopic manifestation of molecular adhesion between cells and provides a quantitative measure for tissue cohesion.<sup>49</sup> Since its introduction by Steinberg, the importance of ATST has been recognized by many others, and several methods to measure it have been devised. The most common is compression plate tensiometry.<sup>48,49,52,54</sup> Using this method, a spherical aggregate is compressed between two parallel plates and is then allowed to equilibrate under the compressive force. During the time that the aggregate settles to its compression equilibrium, the change of force applied to it is recorded.<sup>26,50</sup>

To find the ATST, the equilibrium force and geometrical parameters, such as  $H$  and  $R_1$  (defined in Fig. 1) are recorded. The surface tension can be obtained from  $F/2\pi R_1 = \gamma(\alpha - 1)$ , where the measured equilibrium force is denoted by  $F$ , ATST is denoted by  $\gamma$ , and  $\alpha$  is a unitless quantity obtained numerically by solving an integral equation.<sup>26,50</sup> The slope of the graph ( $F/2\pi R_1$  vs.  $\alpha - 1$ ) provides the ATST in dyne/centimeter. It is worth noting that the relaxation force can be well described in terms of a bimodal process characterized by short and long time components. As can be seen in Fig. 1, when a multicellular spherical aggregate is subjected to compression, the relaxation process can be quantitatively described using a double-exponential fit, with predominantly elastic behavior immediately after compression (short term) and viscous behavior long after the compression (long term).<sup>54</sup> Such an approach helps to study the viscoelastic properties of tissues, and these concepts can be employed to understand the dynamics of multicellular systems. The characteristics of the bioink in extrusion bioprinting are based on these tissue viscoelastic properties.

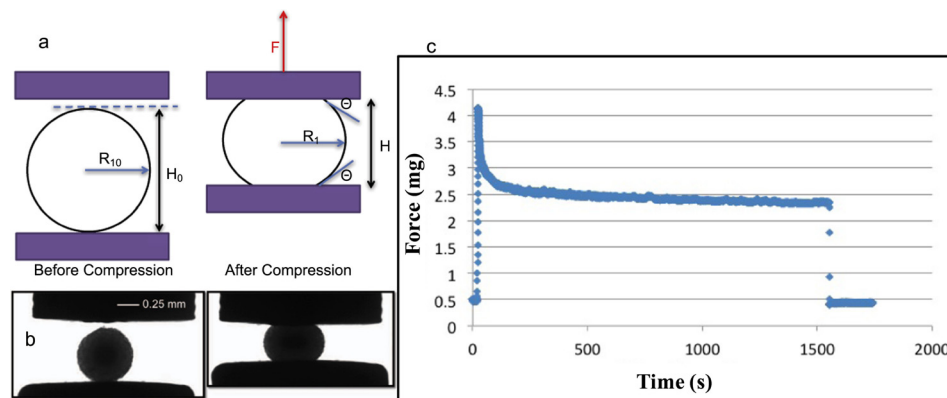


**FIG. 1.** Apparent tissue surface tension (ATST) measurement using a parallel plate compression device and evaluated by the exact solution of Laplace equation (a) Geometrical parameters to calculate the ATST.  $R_{10}$  is the initial radius of the aggregate.  $R_1$  and  $F$  are the (equatorial) radius of the curvature of the compressed aggregates and applied force on the upper compression plate after compression occurred, respectively (b) Snapshots of a spherical aggregate before and after the compression. (c) Typical time relaxation of the post-compressive force acting on the upper plate vs. time. The initial peak in the force vs. time graph represents the moment that the cell aggregate is compressed. The relaxation time for cellular aggregates is typically 1200–1800 s, depending on their composition. The equilibrium force that is needed for the exact solution of the Laplace equation is determined from this diagram. Reproduced with permission from A. Shafiee, C. Norotte, and E. Ghadiri, *Bioprinting* 8, 13 (2017). Copyright 2017 Elsevier.



## Cell sorting

Cell sorting is an early morphogenetic phenomenon that gives rise to compartmentalization in the embryo and eventually the separation between tissues and organs.<sup>40</sup> In particular, when two cell types are randomly mixed in an aggregate, one cell type is sorted into the interior of the aggregate surrounded by the other cell type. The DAH explains this phenomenon as more adhesive cells shift to the interior, thus maximizing their mutual adhesion and minimizing the configurational energy of the assembly [Fig. 2(a)]. The DAH predicts that the more adhesive cells may have a higher ATST; this conclusion has been confirmed in several *in vitro* investigations.<sup>49,51–53</sup>

## Physics of cell sorting

Cell sorting is one of the imperative stages of evolution.<sup>55</sup> It has also been shown that the final sorting equilibrium resembles the phase separation of immiscible fluids both qualitatively and quantitatively. A hierarchical relationship was observed in sorted patterns that was consistent with the values of ATST as predicted by the DAH.<sup>49</sup>

For example, the sorting process of two identical cell populations that only differ in the number of their N-cadherin molecules was studied.<sup>56</sup> The two cell populations were genetically manipulated to express a 50% difference in N-cadherin molecules [Fig. 2(b)]. The difference in the number of N-cadherin cell adhesion molecules (CAMs) caused a marked alteration in tissue behavior, which confirms the establishment of immiscible tissue layers.

To minimize energy during cell sorting, cells with a higher number of CAMs attach to adhesively similar cells; such configuration causes the formation of maximal numbers of CAM bonds (Fig. 2). A random mixture of the two cell types minimizes its energy by cell sorting. Cell movement powered by metabolic energy is responsible for such energy minimization, which in turn is driven by cytoskeletal rearrangement. This cell movement involves breaking and reforming adhesive bonds until the cells find the energetically appropriate partner (energy minimization). The energy for this procedure is proportional to frictional forces involved in the process. Noticeably, the cellular

environment and its corresponding friction coefficient,  $\mu$ , are important factors during cell rearrangement.

## Tissue fusion

Tissue fusion is a self-assembly process in which two or more separate but continuous multicellular assemblies coalesce.<sup>33</sup> Fusion is an essential morphogenetic phenomenon that results in complex arrangements out of simpler ones in early development. It is analogous to liquid droplets fusion,<sup>40</sup> which is resisted by viscosity ( $\eta$ ) and is driven by surface tension ( $\gamma$ ).<sup>57–59</sup> Tissue bioprinting processes that involve high-cell-density printing are heavily reliant on this self-assembly process. The fusion of cellular assemblies can be studied by recording snapshots of aggregates fusing at different time points. The respective snapshot for each time point is analyzed, and geometric parameters are extracted. The fusion of two aggregates and the relevant geometric parameters to determine the fusion time are depicted in Fig. 3. The quantities  $R$  and the  $\theta$  can be used to determine the time course of fusion. The mathematical relationship between  $R$  and  $\theta$  is given as:  $(r/R)^2 = \sin^2\theta \approx 1 - \exp(-t/\tau)$ , where  $\tau$  is the characteristic fusion time ( $\sim\eta/\gamma$ ).<sup>57</sup> Consequently, by recording the evolution of fusion experiment, the essential parameter  $\theta$  can be obtained. Afterwards,  $\sin^2\theta$  vs. time is plotted, and the characteristic fusion time can be found using an exponential fit.

## Physics of tissue fusion

The fourth dimension of bioprinting is the time required for the discrete bioink units to fuse, for cells within the structure to sort, and for the printed construct to mature and eventually be ready for implantation. The multicellular systems or organoids fuse to each other upon placement in the vicinity of each other as would two droplets of a liquid. The fusion process begins with the attachment of the closest cells at the contact point between the two fusing aggregates.<sup>26</sup> These cells start to break contacts with nearby cells and re-form bonds with cells on the surface of the opposite aggregate. These attachments trigger a cascade of cellular attachments along circular areas [Fig. 3(g)]. These circles are numbered sequentially and are denoted by  $L$  and  $R$  for the left and right

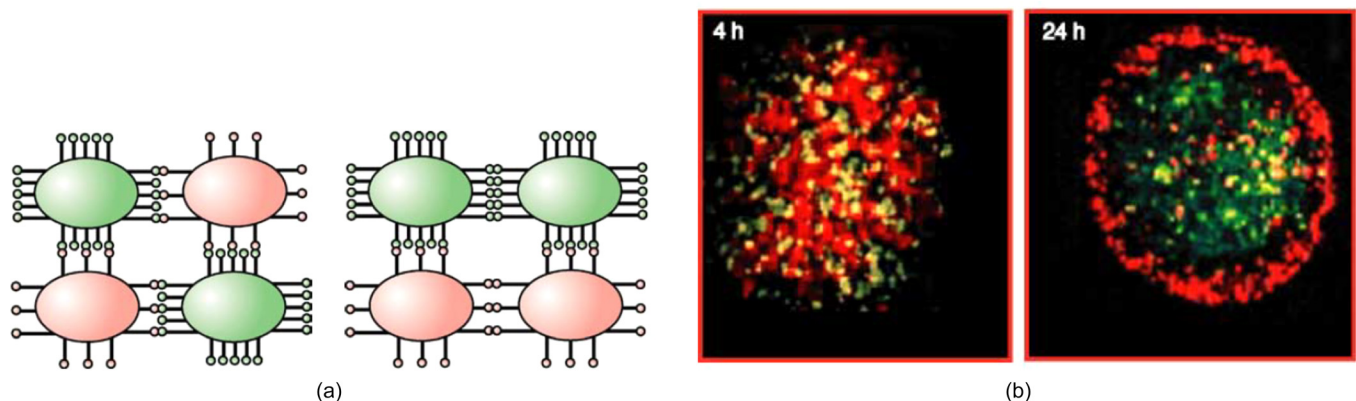


**FIG. 2.** Cell sorting. (a) Schematic illustration of adhesion in a mixture of two cell types with a different expression of homophilic cell adhesion molecules. The cells with higher expression, because of energy minimization, sort in such a way as to be close to cells with higher expression; this allows the cells to use all their available bonds. (b) Sorting procedure—two genetically transformed Chinese hamster ovary cell aggregates with  $\sim 50\%$  variance in N-cadherin expression. Reproduced with permission from G. Forgacs and S. A. Newman, *Biological Physics of the Developing Embryo*. Copyright 2005 Cambridge University Press.

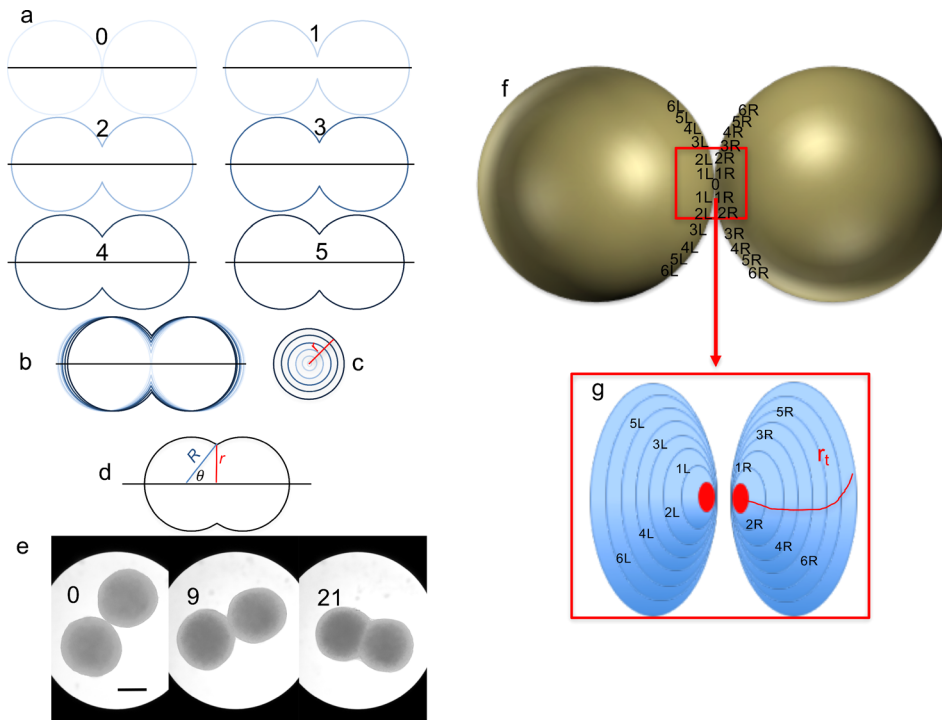


**FIG. 3.** Two touching spherical aggregates fuse together as would two liquid droplets. (a) Schematic of fusion experiment at different times. (b) Overlaps of schematics (0–5) demonstrate the fusion procedure. While the fused area grows, the aggregates grow closer to each other. (c) Circles with increasing radii are the cross-section of the fusion. (d) The geometrical parameters  $R$  and  $\theta$  are used to investigate the fusion mathematically. (e) Snapshots of fusion of two human skin fibroblast cellular bioinks at different time points. (f) Two fusing spherical bioinks; the numbers denote imaginary ribbons in an aggregate. L and R represent ribbons from the right or left aggregate. (g) Upon completion of fusion for each ribbon ( $n$ ), the next ribbon ( $n+1$ ) on the right bioink becomes close to the ribbon ( $n+1$ ) on the left bioink. Reproduced with permission from A. Shafiee, C. Norotte, and E. Ghadiri, *Bioprinting* 8, 13 (2017). Copyright 2017 Elsevier. For additional details, see Refs. 26 and 58–60.

aggregates, respectively. Each circle has an area of  $\pi r_t^2$  on which a different number of cells are located. The circle radius  $r_t$  is a time-dependent quantity. The advancement of fusion implies increasing  $r_t$ -s that in turn implies a larger number of cells forming contacts between the two aggregates. The fusion continues by the attachment of sequential circles. At any given time-point, cells in the cross-sectional area of  $\pi r_t^2$  are attached to each other. For cylindrical bioinks, the fusion process consists of a cascade of cell attachments along rectangular contact areas.<sup>60</sup>

### TISSUE MATURATION ACCELERATION

Time is a critical factor during autologous organ printing, and patients who are potential recipients of such organs may benefit from the acceleration of the steps required in the printing process, from cell isolation to proliferation, bioprinting, and implantation.<sup>26</sup> The fusion of bioinks is an example where acceleration may be achieved through a deep understanding of the underlying physics.

It has been shown that faster bioink fusion is feasible by tuning the ATST of bioinks.<sup>26</sup> Hence, in accelerating the post-bioprinting tissue maturation, ATST has been introduced as a measurable biomechanical property to optimize the preparation of cellular bioinks. Using two different preparation methods, multicellular spherical aggregates were fabricated as cellular bioinks. The biomechanical properties of cellular bioinks as evaluated by the ATST, as well as the characteristic fusion time, strongly depend on the method of preparation. Moreover, the cellular bioinks with the higher ATST fused faster; this accelerated the post-printing maturation of the bioprinted construct. Thus, ATST can be used as a measurable biophysical parameter for bioprinting technology to select the cellular bioink.

The fusion process as microscopically observed is shown in Fig. 3. The dissimilarity between bioinks with diverse ATSTs (i.e.,  $\gamma$ ) stems

from their adhesive molecules. In other words, the fact that higher ATST translates into faster fusion reflects greater cohesion among the cells that comprise the bioinks. It has been shown that ATST manifests cohesive and adhesive interactions; therefore, surface tension can be expressed in terms of effective binding energy among cell adhesion molecules ( $J$ ) and their number per unit area:  $\gamma \approx JN$ .<sup>54,61</sup> Aggregates therefore show higher surface tensions when they are composed of cells with a higher number of contacts and stronger adhesive bonds.<sup>52</sup> Cells in aggregates with a higher ATST bind to each other more strongly than cells in aggregates with a lower ATST.<sup>26</sup> The stronger bond that develops between cells in aggregates with higher ATST causes these initial cells to achieve their equilibrium position faster. Conversely, cells in an aggregate with lower ATST reach their new position at a slower rate. (Mathematically, the fusion time,  $\tau$  is inversely proportional to ATST ( $\gamma$ ). Thus, the higher the  $\gamma$  is the smaller the  $\tau$  is and the faster the fusion is.) Furthermore, the new equilibrium position for attached cells is closer for higher ATST aggregates. The closer proximity of cells in higher ATST aggregates additionally indicates higher cell-density that increases the chance of attachment and accelerated fusion. Moreover, to study the fusion mathematically, the cell attachments, based on cell adhesion molecules, were modeled using a series of zippers.<sup>60</sup> By solving the partition function of the respected statistical mechanical model, the total energy involved in the fusion of two bioink particles could be determined

$$\langle E \rangle_{total \text{ for sph}} = \frac{2\pi r}{\kappa} \langle E \rangle = \frac{-2\pi r}{\kappa} \left( \frac{\varepsilon(N+1)e^{-(N+1)\beta\varepsilon}}{1 - e^{-(N+1)\beta\varepsilon}} + \frac{\varepsilon e^{-\beta\varepsilon}}{1 - e^{-\beta\varepsilon}} \right)$$

$$\langle E \rangle_{total \text{ for cyl}} = \frac{2\ell}{\kappa} \langle E \rangle = \frac{-2\ell}{\kappa} \left( \frac{\varepsilon(N'+1)e^{-(N'+1)\beta\varepsilon}}{1 - e^{-(N'+1)\beta\varepsilon}} + \frac{\varepsilon e^{-\beta\varepsilon}}{1 - e^{-\beta\varepsilon}} \right),$$

where  $k$ ,  $l$ , and  $r$  are the distance between subsequent adhesive molecules, length of cylindrical bioink, and radius of spherical bioink, respectively, whereas  $N$  and  $N'$  are the number of cell attachments in spherical and cylindrical fusion, respectively, and  $\varepsilon$  is the energy of one cell attachment (i.e., a pair of bound cell adhesion molecules).

The energy of fusion can be employed to optimize the post bioprinting maturation process that is critical for the final product.

## TISSUE MATURATION MODELING

### Cellular particle dynamics

Once cells are printed, they relocate and reorganize to self-assemble into a mature functional construct potentially ready for implantation. At the same time, the extended keeping of the construct in the bioreactor may lead to a decrease in its functionality (e.g., due to necrosis or another type of cell death). Thus, the post-printing maturation process that takes time (the fourth dimension) needs to be optimized. Optimization can be facilitated through predictive modeling, an approach still rarely used in tissue engineering. To this end, a theoretical, experimental, and computational framework, the Cellular Particle Dynamics (CPD), was introduced using the physics of multicellular systems to quantitatively model post-printed shape evolution.<sup>57</sup> Here, we briefly describe the key aspects of CPD.

To predict the biomechanical relaxation of multicellular systems, CPD is used as a computer simulation framework<sup>57–59</sup> in which a cell is studied as a continuum material object with a flexible shape and constant volume and is coarse-grained into a finite number of equal volume elements. Point-like cellular particles (CPs) that represent these elements are located at the elements' center of mass. CPs in an individual cell and/or in different individual cells interact via attractive and repulsive forces and are locked together by a restricting potential that effectively simulates a cell membrane. The effective size of a CP is determined by the superposition of the repulsive and attractive interactions. The cell's shape is ultimately determined by these CPs' motion that is described by over-damped Langevin dynamics. The time-dependent shape evolution of the multicellular system can be studied by finding the trajectories of all CPs through the integration of their equations of motion. The initial values of the relevant parameters are chosen using calibration experiments. Simulations using CPD, when compared with experiments, correctly predicted the time evolution of a number of post-printing fusion processes with spherical and cylindrical multicellular bioinks. With this framework, the dynamics of multicellular systems (printed using either spherical or cylindrical cellular bioinks) can be predicted and optimized.

Despite the successful modeling of the post-printed maturation process using CPD, a word of caution is due here. CPD is fundamentally a computer simulation. Thus, even if it uses as input theoretical considerations about the multicellular system and experimental data, at best it describes a system that is analogous but not identical to the true biological structure it targets to model.

## PHYSICS OF EXTRUSION BIOPRINTING

The bioinks used with extrusion printing are typically viscous hydrogels, with or without cells, forced through a nozzle pneumatically or mechanically. Purely cellular bioinks printing was discussed above; in this section, we concentrate on cell-laden biomaterials or cell-less materials. The nozzle is moved at a specified height over the substrate or preceding layer of the material as the bioink is dispensed. The

resulting flow of bioink has a physical form dependent on the hydrogel's rheological properties and dispensing conditions including nozzle diameter ( $D$ ), dispensing height ( $h$ ), translation speed ( $F$ ), volumetric flow rate ( $Q$ ), and adhesion to the substrate. The rheological properties of the bioink not only affect flow dynamics as the material is extruded but also impact the 3D shape retention after extrusion. This section focuses on collating published approaches to modeling these properties and conditions mathematically.

The dispensing conditions impact the quality of the print, cell viability, and total print time. The nozzle diameter impacts the resolution and speed of printing due to its minimum feature size. The dispensing height governs the height of each layer above the receiving surface, whether the surface is a substrate (such as a petri dish or glass slide) or the previously dispensed layer of material. Altering this height impacts the number of layers and the cross-sectional shape of the dispensed material. The translation speed defines the speed of the nozzle relative to the substrate.

Current printability definitions have a targeted physical form of stable, stackable filaments that are highly repeatable and predictable. In reality, bioinks can be highly variable in physical form depending on the concentrations of hydrogel and cellular components. The form for a given bioprinting application should be determined by the user and tailored to the desired outcome. The goal is to understand the interactions between bioink properties and extrusion parameters such that the bioprinting process results in the designed outcome. The outcome may be one of the precisely defined filaments stacked with well-defined pores and interfaces. Alternatively, the outcome may be a spatial organization of cells within a hydrogel of intentionally low stiffness which will not maintain well-defined architecture but is better suited for cell viability or differentiation along a specific lineage. The goals of studying the physics of bioink printability are to understand the bioink extrusion characteristics in order to achieve reproducible and predictable results and to develop improved bioinks that have enhanced architectural capability while preserving dependable extrusion and cell culture dynamics.

Extrusion dynamics are typically modeled with hydrogels such as poloxamer 407, alginate, alginate/gelatin, and others that can produce reliable and repeatable results with high shape fidelity.<sup>62</sup> Although these models have provided a better understanding of the factors that control the bioprinting process, these gels have specific limitations and are not truly representative. Bioink characteristics that are important to the extrusion process include dynamic viscosity, loss modulus, and storage modulus. Shear stress and applied pressure must also be controlled to preserve cell viability. Therefore, it is important to understand the relationships between flow rate, shear stress, applied pressure, moduli, and viscosity when planning a bioprinting approach.

Bioink performance depends in large measure on the extrusion context as well as the inherent rheological properties. Relevant mathematical relationships and models that are helpful in modeling the microextrusion of materials are discussed below, bearing in mind that there are many ways to improve on these models and fill knowledge gaps.

### Newtonian and non-newtonian fluid dynamics

Few materials in the bioprinting repertoire can be classified as Newtonian fluids, so most bioinks will not be modeled using classical



relationships. However, for simplified calculations and estimations, or for materials with properties that are close to Newtonian, the equations for ideal Newtonian fluids have proved useful. The ease of modeling Newtonian fluids is due to the direct, linear relationship between an imposed force and the resulting flow; this direct relationship results in a constant viscosity at a given temperature and atmospheric pressure. Contrarily, non-Newtonian fluids have a viscosity that is a function of the imposing force to create flow, which results in a complex relationship between the imposing force and the resulting fluid flow.

The objective of the discussion below is to briefly review how basic concepts of fluid dynamics can be used to define printability of a given material.

For a Newtonian fluid in laminar flow conditions,<sup>63</sup> the Hagen-Poiseuille equation relates the volumetric flow rate ( $Q$ ) to the pressure ( $P$ ) applied to a nozzle (of length  $L$  and diameter  $d$ ) and viscosity ( $\eta$ )

$$Q = \frac{\pi \Delta P}{128 L \eta} d^4.$$

This equation can be used to estimate the bioink viscosity, provided all the other quantities are known or measurable (in particular the flow rate). Combining the Hagen-Poiseuille equation with conservation of volume ( $V$ ) (not restricted to Newtonian fluids but regularly assumed<sup>64</sup>) successful models of dynamic flow systems can be built that relate the nozzle cross-section area ( $A$ ), flow velocity ( $v$ ), and time ( $t$ ), to flow rate.

$$V = Avt = Qt. \quad (1)$$

Shear stress ( $\tau$ ) in Newtonian fluid flow is linearly related to the shear rate ( $\dot{\gamma}$ ) or the velocity gradient by the material viscosity ( $\eta$ ), assumed to be a material constant<sup>65</sup>

$$\tau = \eta \dot{\gamma}. \quad (2)$$

Shear stress is a feature of fluid flow where the flow encounters friction with a parallel boundary, and a velocity gradient becomes orthogonal to the direction of the generated flow. The internal force is distributed across the cross-sectional area in the plane of flow.

The shear rate for Newtonian bioinks can be related to the nozzle's internal radius ( $R$ ) and average flow velocity ( $\bar{v}$ ).<sup>28</sup> [the latter can be estimated from Eq. (2) above]

$$\dot{\gamma} = \frac{4\bar{v}}{R}.$$

Shear stress in non-Newtonian fluids can no longer be expressed in terms of constant viscosity [as in Eq. (2) above] since the apparent viscosity becomes a function of the shear rate. Shear thinning is the phenomenon of some non-Newtonian fluids to experience a reduction in apparent viscosity with the increasing shear rate. Most aqueous mixtures of biological materials exhibit shear thinning behavior, and thus, it is relevant to bioink extrusion. Consequently, if the bioink has obvious shear thinning behavior (as most often the case), the oversimplification represented by the above equations that apply strictly to the Newtonian fluid may lead to misleading results. Nevertheless, they still may provide helpful information when estimating the theoretical extrusion volume in terms of rheological properties attained prior to printing.

The functional relationship between the apparent viscosity and the shear rate can be expressed in terms of a Power Law equation

$$\eta = K \dot{\gamma}^{n-1}.$$

Here,  $\eta$  is the apparent viscosity,  $K$  is the viscosity factor, and the exponent  $n$  is the shear thinning factor.<sup>28,65–67</sup> Thus, Eq. (2) is modified as

$$\tau = K \dot{\gamma}^n. \quad (3)$$

The Power Law equation represents a simple model to understand the complex relationship between the shear rate and the shear stress in non-Newtonian fluids in terms of a scalar (viscosity factor) and exponential (shear thinning factor).

The Power law equation allows us to determine the shear stress and the velocity profile across the nozzle radius and average extrusion velocity<sup>28,68</sup> in terms of measurable quantities characterizing the non-Newtonian flow. Shear stress ( $\tau_r$ ) and fluid velocity ( $v$ ) are expressed as functions of the distance ( $r$ ) along the radius ( $R$ ) determined by the shear rate and viscosity discussed above

$$\tau_r = \frac{r \Delta P}{2l},$$

$$v = \frac{n}{n+1} \left( \frac{\Delta P}{2LK} \right)^{\frac{1}{n}} \left( R^{\frac{n+1}{n}} - r^{\frac{n+1}{n}} \right).$$

The average velocity ( $\bar{v}$ ) can be evaluated as well by averaging across the entire radius ( $R$ )

$$\bar{v} = \left( \frac{-\Delta P}{2LK} \right) \left( \frac{n}{3n+1} \right) R^{\frac{n+1}{n}}.$$

The printability of a given biomaterial depends on the properties of the bioink (its apparent viscosity); thus, as the above discussion illustrates, the applicable flow conditions (intended geometry, printing parameters) that might be complex. Many of the relevant parameters have ranges within which the material will be extruded and narrow regimes that could be defined as printable. Thus, it is not surprising that even if definitions of printability have been under development for some time,<sup>65,69,70</sup> there is no consensus to date.

One approach to determine the quality of material extrusion is to assess the relevant parameters post-bioprinting. Researchers have taken measurements of filament consistency, filament cross-section, cross-hatch lattice quality, and stacking stability to express a semi-quantitative measure of printability.<sup>62,64,65</sup> A flaw in such an approach is that no material can be evaluated simply on the basis of its material properties in order to predict its printability, since material properties are strongly dependent on flow conditions, as demonstrated by the above analysis.

Recognizing this, Gao *et al.* have recently evaluated printing dynamics and the resulting filament properties, which they subsequently related to the material's rheological dynamic moduli.<sup>71</sup> Using the relationships to define viscosity in terms of loss modulus ( $G''$ ), storage modulus ( $G'$ ), and the loss tangent ( $\tan \delta$ ) of the material

$$\eta = \frac{(G'^2 + G''^2)^{1/2}}{\dot{\gamma}'},$$



$$\tan \delta = \frac{G''}{G'}.$$

The authors determined a printable range for gelatin, alginate and their mixtures. They admit that their analysis does not account for other rheological properties that must be incorporated (e.g., yield stress), but in the model system used, a  $\tan \delta$  range of 0.25 to 0.45 was found to exhibit good printability.

### Pneumatic extrusion

Pneumatically actuated printing is commonly used because of the non-contact nature of motive force delivery. In this technique, the motive force is produced by a pressure differential generated by air introduced into the material reservoir. Understanding the bioink properties is important to relate pressure to the flow rate. With non-Newtonian fluids, like most bioink materials, the relationship is strongly dependent on the rheological properties of the bioink.<sup>69</sup> The equations provided in this section are helpful in approximating the relevant relationships; however, the factors that complicate these relationships require further elucidation.

There is evidence that pressure above a certain threshold can have a negative effect on cell viability, independent of shear stress.<sup>72</sup> Therefore, it is helpful to have accurate models for estimating the necessary pressure for adequate flow rates; low flow rates may negatively influence cell viability, while high flow rates may enhance cell damage due to high shear rates.

### Mechanical extrusion

In mechanically actuated systems, the flow of the material is driven by volumetric displacement generated by a piston or screw. The dependence of the extruded volume on the flow rate is straightforward due to the conservation of mass, allowing the piston velocity to directly relate to extrusion velocity via the ratio of cross-sectional areas. However, the time required for the extruder to build sufficient pressure to overcome the yield stress of the bioink is an important consideration that requires optimization and tuning of timing, acceleration, and/or extruder reversal in order to have appropriate extrusion at the start- and end-points of a printed filament.<sup>68</sup>

## PHYSICS OF INKJET PRINTING

Inkjet printing is well-known owing to its diverse range of applications, including printed electronics,<sup>73–75</sup> energy conversation,<sup>76,77</sup> material deposition,<sup>21,78</sup> and bioprinting.<sup>79,80</sup> The advantages provided by inkjet printing such as computer-aided patterning, high resolution, and cost-effective deposition make this technique advantageous for many uses.<sup>19,76</sup> Following the application of inkjet printers to bioprinting for tissue engineering,<sup>79</sup> regenerative medicine,<sup>79,81</sup> biosensing,<sup>4</sup> and drug delivery,<sup>5</sup> the range and number of materials printed by inkjets have dramatically increased.<sup>23</sup>

In this technique, the most important issue in the pre-printing process is ink printability. To ensure that the bioink material can be dispensed from the nozzle orifice and reach the substrate for deposition, the interaction of ink, the nozzle, substance, and orifice diameter and shape must be considered. The printing process can involve different actuators (piezoelectric or thermal); however, these share dominant parameters that utilize common equations and the physical

concepts behind them. After the impact of the droplet with the substrate, the interaction between the bioink droplet and the solid surface is of utmost importance, affecting kinematics, spreading, relaxation, wetting, and equilibrium phases;<sup>82,83</sup> the droplet's shape and impact speed as well as surface wettability are critical parameters for drop impact and spreading. The moment that the drop collides with the surface is governed by kinematic behavior and lasts for  $<1 \mu\text{s}$ .<sup>84</sup> When the droplet collides with the solid surface of the substrate, six different scenarios may ensue: deposition, prompt splash, corona splash, receding breakup, partial rebound, and complete rebound.<sup>85</sup> Among all these possible outcomes, deposition is the only favorable setup to deliver layers of materials for bioprinting purposes. These scenarios are dependent on the ink properties and surface characteristics; for example, rebound is highly likely to occur on superhydrophobic surfaces or if the kinetic energy of the drop is too high and the surface energy is low.

After the kinematic phase, the droplet on the surface undergoes spreading: the droplet expands as far as its initial kinetic energy permits. While a higher impact speed or bigger droplet increase the speed of spreading, higher surface tension or viscosity slows down the process. The spreading phase is followed by the relaxation phase during which the drop (upon reaching its maximum diameter) experiences relaxation with an oscillation in its shape on the surface. The equilibrium contact angle  $\theta_{eq}$  defines how far a droplet can wet the surface. In other words, the largest diameter a droplet can attain after spreading and relaxation reflects the wettability of the surface. This equilibrium condition is based on the minimum of the surface energy.

The surface properties of materials such as surface energy show interesting differences with materials in bulk.<sup>85</sup> Atoms in the bulk structure (internal structure) are surrounded by other similar entities and experience the same force in a 3D matrix. In contrast, atoms at the surface of the material and in its outermost layer are attracted by forces on one side toward the interior of the material. Thus, the energy balance of the surface is dissimilar to its counterpart inside the material. This phenomenon leads to the surface layer possessing a higher energy than the bulk material and is referred to as surface energy (with a unit of energy per unit of area). To avoid confusion, surface energy is used for the situation in which the material is located in the vacuum, while interfacial free energy is used when studying the behavior of the material in other mediums.<sup>33</sup> It is worth noting that all materials, including droplets on a solid surface, tend to minimize their energy. Therefore, the contact angle may vary depending on the substrate surface and ink properties. It has been shown that when the surface energy is too high, the droplet tries to minimize the energy and spreads to a maximum possible distance, creating a very low contact angle; these surfaces are hydrophilic. On the other hand, for a surface with very low energy where the liquid does not spread (since that would increase its total energy), the droplet may form spherical shapes; such surfaces are hydrophobic. It has been shown that  $\gamma_{sv} = \gamma_{sl} + \gamma_{lv} \cos \theta$ , where,  $\gamma$ ,  $s$ ,  $v$ , and  $l$  denote the surface energy, solid, vapor, and liquid, respectively, and  $\theta$  is the contact angle.<sup>86</sup> The interfacial energy between liquid and vapor ( $\gamma_{lv}$ ) is the surface tension of the ink. It is obvious that for hydrophobic surfaces,  $\gamma_{sv} = \gamma_{sl}$  and for hydrophilic surfaces,  $\gamma_{sv} = \gamma_{sl} + \gamma_{lv}$ .

### Fluid properties for bioink printability

The mechanisms of drop formation and fluid properties are critical factors that need to be optimized for the desired outcome in inkjet

printing. Many bioinks may fulfill biocompatibility criteria but fail because their fluid properties are not appropriate for inkjet printing. In inkjet printers, the ink is ejected from a nozzle by an actuator (either piezoelectric or thermal<sup>77</sup>). In a thermal inkjet printer, a heater generates a bubble in the ink reservoir and ejects it from the orifice.<sup>87</sup> In a piezoelectric printer, the ink droplet is ejected through the changes in the shape and size of a piezoelectric crystal generated by a voltage pulse. The printing behavior (droplet shape, size, and velocity) is strongly dependent on the shape and amplitude of the actuating pulse.<sup>88</sup> Therefore, it is always important to optimize the actuator pulse prior to printing. A droplet can be ejected from the nozzle with a tail (known as satellite) that would decrease the deposition quality afterward.<sup>74,89,90</sup> Obtaining a satellite-free droplet or one of the minimum lengths is imperative for the optimization of the actuator pulse. The velocity of the droplet may also be defined by an actuator pulse. In addition to the velocity of the droplet, density, viscosity, and surface tension are also important parameters that must be tested prior to designing the experiment with each new specific bioink. Here, we present a group of useful quantities that define the printability of a liquid and reveal necessary information about the ink: (Reynolds)  $Re = \frac{v\rho a}{\eta}$ , (Weber)  $We = \frac{v^2 \rho a}{\gamma}$ , and (Ohnesorge)  $Oh = \frac{\sqrt{We}}{Re} = \frac{\eta}{(\gamma \rho a)^{1/2}}$ .

In these expressions,  $a$  is a characteristic length. In addition, fluid properties are used and denoted by  $\rho$ ,  $\eta$ , and  $\gamma$  which represent the density, dynamic viscosity, and surface tension of the fluid, respectively.<sup>84</sup> Any stable droplet can be obtained from a liquid with  $1 < Z = 1/Oh < 10$ . Therefore, finding the  $Re$ ,  $We$ , and  $Oh$  numbers and optimizing them based on the  $1 < Z < 10$  condition can help to obtain a bioink suitable for inkjet printing. This condition may give some constraints on density, viscosity, and surface tension to tailor a suitable bioink. Bioinks with small  $Z$  values ( $< 1$ ) cannot be printed because their viscous dissipation prevents drop ejection. On the other hand, bioinks with high  $Z$  values ( $> 10$ ) will produce a large number of unwanted satellite droplets.<sup>84</sup>

In addition to  $Re$ ,  $We$ , and  $Oh$ , numbers that are generally related to the fluid properties, inertial, capillary, and gravitational forces should be taken into account for printing purposes. The capillary number  $Ca = \frac{\eta v}{\gamma}$  relates the effect of viscous forces to surface tension acting across an interface, whereas the Bond number  $B_0 = \frac{\rho g L_0^2}{\gamma}$  represents the effect of gravity that can be neglected in most cases for small droplets (which is the case for inkjet printing).<sup>91</sup> In these expressions, the yet undefined quantities are  $L_0$ ,  $v$ ,  $\eta_0$ , and  $g$ , respectively, a characteristic length (such as drop diameter), the fluid's speed, its low-shear viscosity, and the gravitational constant.

$We$  and  $Oh$  can be used to characterize the dynamics of spreading.<sup>92</sup>  $We$  is the ratio of inertial forces to capillary forces; therefore, a

high  $We$  number implies that impact-induced inertia is the influential parameter in the dynamics of a spreading drop, and a low  $We$  indicates that the capillary forces prevent the drop from spreading.<sup>93</sup> The  $Oh$  number is based on fluid properties and the size scale and can compare viscous forces with surface tension forces. A high  $Oh$  number indicates that viscosity is playing a major role in drop spreading, while a bioink with a low  $Oh$  number indicates that surface tension is playing the dominant role. The latter situation is usually the case for inkjet printing where the spreading is dominated by interfacial forces.<sup>93</sup>

## PHYSICS OF LASER ASSISTED BIOPRINTING

Laser-assisted bioprinting is a nozzle-less printing approach and is generally comprised of three parts, a laser, a focusing system that keeps the laser beam aligned and focused, and a ribbon layer that aids in absorbing and transferring energy to the cells. The ribbon is usually made of gold, silver, or titanium. The substrate faces the ribbon and is positioned a few hundred microns away from it. This setup permits the precise focusing of the laser beam on the ribbon, onto which a thin layer of cellularized ink is spread. The energy created by the laser beam generates a cavitation that thrusts a cell-containing droplet onto the receiving end, where the substrate is located.<sup>94–99</sup> This technique does not transfer mechanical stress to the cells, resulting in high cell viability. Furthermore, laser bioprinters can also be used to print highly viscous materials, hence covering a broader range of bioinks than that possible with inkjet printing. However, the adverse impact of the laser beam on the cells is not thoroughly known. In addition, laser-based systems are more expensive than other techniques. Moreover, the fabrication speed of laser bioprinting is medium compared to inkjet bioprinting.<sup>19,94</sup> Laser-induced forward transfer (LIFT) is a type of bioprinting comprising a transplant solid plate, an absorbing layer, and a thin liquid film containing the bioink.<sup>94–100</sup> The LIFT setup, schematically shown in Fig. 4, consists of a laser beam facing the rear side of a ribbon coated with the cellular material. Laser pulses irradiate the absorbing matrix of the coating, thereby creating extremely localized heating a vapor bubble is evaporated at the interface of bioink coating and the quartz disk. Next, the vapor bubble develops quickly and is expelled onto the target surface. Subsequently, the bubble may be ejected as a droplet for further deposition or patterning.

Irrespective of the presence or absence of an initial bulgy shape, the product of the jet might break up before impacting onto the substrate.<sup>101</sup> This can be delineated in terms of the direct writing height (DWH) and the breakup length. In the former case, the breakup length is either smaller than or equal to the DWH, which results in droplet-impingement printing. The latter leads to jet-impingement printing, which is associated with single or several breakups; in these

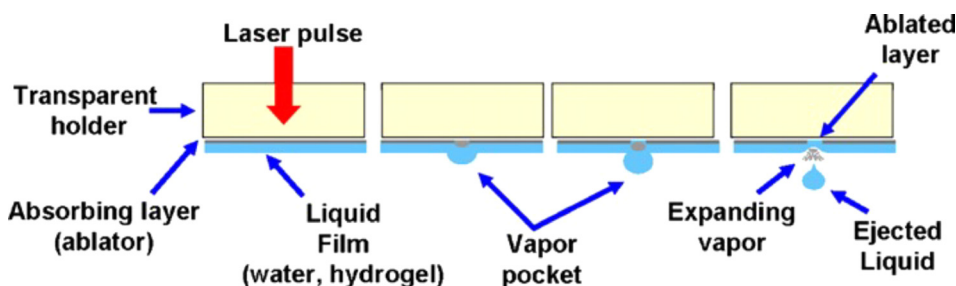


FIG. 4. Schematic of LIFT bioprinting. Reproduced from C. Mézél, A. Souquet, L. Hallo, and F. Guillemot, *Biofabrication* 2, 014103 (2010). Copyright 2010 Institute of Physics.

breakups, the breakup length is larger than the DWH.<sup>102</sup> The Weber number is a parameter that is determined by calculating the ratio of the liquid inertia-to-surface tension in the process of impingement. The critical Weber number ( $We_c$ ) is used to designate when splashing occurs, the parameter  $We_{t1}$  is used to designate the threshold for material transfer, and the parameter  $We_{t2}$  is used to designate the threshold for material transfer with pluming, splashing, or bulgy shape. The condition for splashing on the substrate to occur can be expressed as " $We \geq We_c$ ." There are several scenarios reported on the ranges of the Weber number. For a situation in which  $We < We_{t1}$ , the pressure in the bubble is inadequate to surpass the surface tension of the coating and the surrounding pressure; consequently, the ink material is unable to escape as a jet droplet. For situations in which  $We > We_{t2}$ , the pressure on the bubble is too high; it bursts and either splashes or forms a jet with a bulgy shape. For situations in which  $We_c < We < We_{t2}$ , the splashing phenomenon becomes relentless. All of the scenarios described above should be avoided, and the optimized printing condition is anticipated to occur when  $We_{t1} < We < We_c$ . This is further elucidated by the algorithm shown in Fig. 5, which supports our analysis of laser printing provided by Zhang *et al.*

In the case of laser bioprinting of alginate, it was shown that most of the laser input energy is expanded in the form of elastic, surface, and kinetic energies to form the drops.<sup>103</sup> When a droplet is created, it dissipates becomes of the amalgamation of ambient aerodynamic, capillary, elastic, liquid inertial, and viscous forces. The droplet may experience four different sorts of breakup processes: atomization, first wind-induced breakup, second wind-induced breakup, or Rayleigh breakup processes. Most droplet breakups are extrapolated to either Rayleigh or Plateau-Rayleigh instability. During the creation of the jet (a) capillary thinning and (b) breakup of free surface viscoelastic liquid filament breakup are understood over three time scales: the visco-capillary time scale  $t_v = \eta_0 R / \sigma$ , the Rayleigh capillary scale (which can be mathematically defined as  $t_c = (\rho R^3 / \sigma)^{1/2}$  and  $\lambda$ , where  $\eta_0$  is the zero shear viscosity,  $R$  is the characteristic length considered the laser spot radius, and  $\rho$  symbolizes the density). The Ohnesorge number  $Oh = t_v / t_c = \eta_0 (\rho \sigma R)^{1/2}$ , elasto-capillary number  $E_c = \lambda t_v = \lambda \sigma / \eta_0 R$ , and Deborah number  $De$  (where  $De_0 = \lambda / t_c = (\lambda 2 \sigma / \rho R^3)^{1/2}$ ) are critical numbers to optimize the printing parameters. The afore-mentioned dimensionless numbers are meant for three types of material properties and can be acquired from the corresponding essence of the 3 main rudimentary scales. The prediction of droplet formation can be enhanced using the  $Oh$  and  $E_c$  numbers. The  $E_c$  number alone is inconsequential, but the  $De$  number together with its idiosyncratic processing time is meant for fluids for which viscosity is of paramount importance. Furthermore, the Weber number  $We = \rho R U^2 / \sigma$  is recommended as a process-dynamics figure for the apprehension of jetting dynamics. The  $E_c$  number decreases or the  $Oh$  number increases, and the alginate concentration also increases, which in turn augments the  $We$  number.<sup>103</sup>

In laser bioprinting of mesenchymal stem cells, a transition from a sub-threshold phenomenon to a jetting phenomenon was observed.<sup>25</sup> The slow jets use lower energy and have been able to produce a smooth and stable output. The droplet creation threshold might be understood by utilizing a geometrical explanation encompassing a vertex angle. For the jetting phenomenon, an early enlargement of the bubble, a sudden reduction in the vertex angle, and an inflation of the height, volume, and velocity imply that the initial impulse drives

forward the bioink at a high rate to suppress the critical angle. The vertex angle is a time-dependent quantity and counts on the M.S. Longuet-Higgins equation that is based on the Dirichlet hyperboloid

$$2\Theta = 2\arctan(2^{1/2}/(\tau - \tau_0)^{3/2}[1 + 3/8(\tau - \tau_0)^{-3}])$$

where  $\tau_0 = -1.2936$  and  $\Theta$  = vertex angle.

It was also found that the volume of the exuded fluid can be plotted against the volume irradiated, and the bubble volume is calculated by the empirical relation  $T_c = 0.915 R_{\max} \sqrt{(\rho/P_0)}$ , where  $\rho$  = density =  $10^{-3}$  kg m<sup>-3</sup>,  $P_0$  = 1 atm,  $T_c$  = bubble collapse time, and  $R_{\max}$  = maximum bubble radius.<sup>25</sup>

It has also been shown that there is an applicability between the printed droplet diameter and its volume, which has the following notation as the volume of a spherical segment:<sup>104</sup>  $V_{\text{droplet}} = \pi/3 * a^3 * \sin \theta - 3(1 - \cos \theta)^2 * (2 + \cos \theta)$  with  $a$  being the radius of the contact area and  $\theta$  the contact angle. The printed droplet volume depends on other parameters like pulse duration, pulse energy, and peak power. The dependency is linear; nevertheless, it is not proportional to the pulse energy involved in printing a droplet of a specific volume and the duration of the pulse. This is adopted using the following formula:

$$E_{\text{pulse}} = E_0 + m * \tau_{\text{pulse}} \text{ where } \tau_{\text{pulse}} \text{ is pulse duration.}$$

The laser pulse peak power is proportional to the quotient of laser pulse energy and its duration, the required peak power is measured by  $P_{\text{peak}} \sim (E_{\text{pulse}}/\tau_{\text{pulse}}) + m$ .

In order to attain the same droplet volume with varied pulse durations, there is a rise in the energy level linearly and not proportionally as per the above formula. Nonetheless, the peak power decreases inversely, while the minimum peak power remains constant. At shorter pulse durations, the droplet volume is rapidly amplified with the inflation of the laser pulse energy and not via increasing shear forces. This shows that the pulse energy can be maximized by keeping the intensity constant and by increasing the focal spot size.

A femtosecond laser, in an abstract sense, is contemplated as the cold process ascribable to an ultra-short pulse duration that can be deployed for LIFT. The femtosecond lasers are preferred to other lasers because of the non-linear trait of absorption, which hinders any modification of the focal volume. The absorption is not a material-dependent property and can, therefore, be applied to broader types of materials, enabling devices to be developed as a compound of the substrate of diverse materials. The requirements for optimal femtosecond laser bioprinting are illuminated by the numerical aperture and the precision of whereabouts of the focal spot for different bioinks. The Zernike polynomial for spherical aberration is stated as  $Z_9 = \lambda * (6p^4 - 6p^2 + 1)$ . Here,  $p$  is the normalized radius of the pupil of the system. The longitudinal spherical aberration is linked to the aberrant wavefront with  $Z_9$  by using the given mathematical component  $1 * NA^2/4 = 6 * Z_9/n$ ; in this equation,  $n$  is the optical index of the medium and  $NA$  is the numerical aperture.<sup>105</sup> The femtosecond pulse laser generates spatially well-defined jets with minimal volume at a small height with a stable velocity. Conversely, the picosecond pulse laser generates less-stable jets both in time and energy, and the droplets are sprayed and are rendered unsuitable for printing in various applications.<sup>106</sup> It is inferred from this work that there exists a non-linear relationship between hydrogel viscosity and droplet volume.

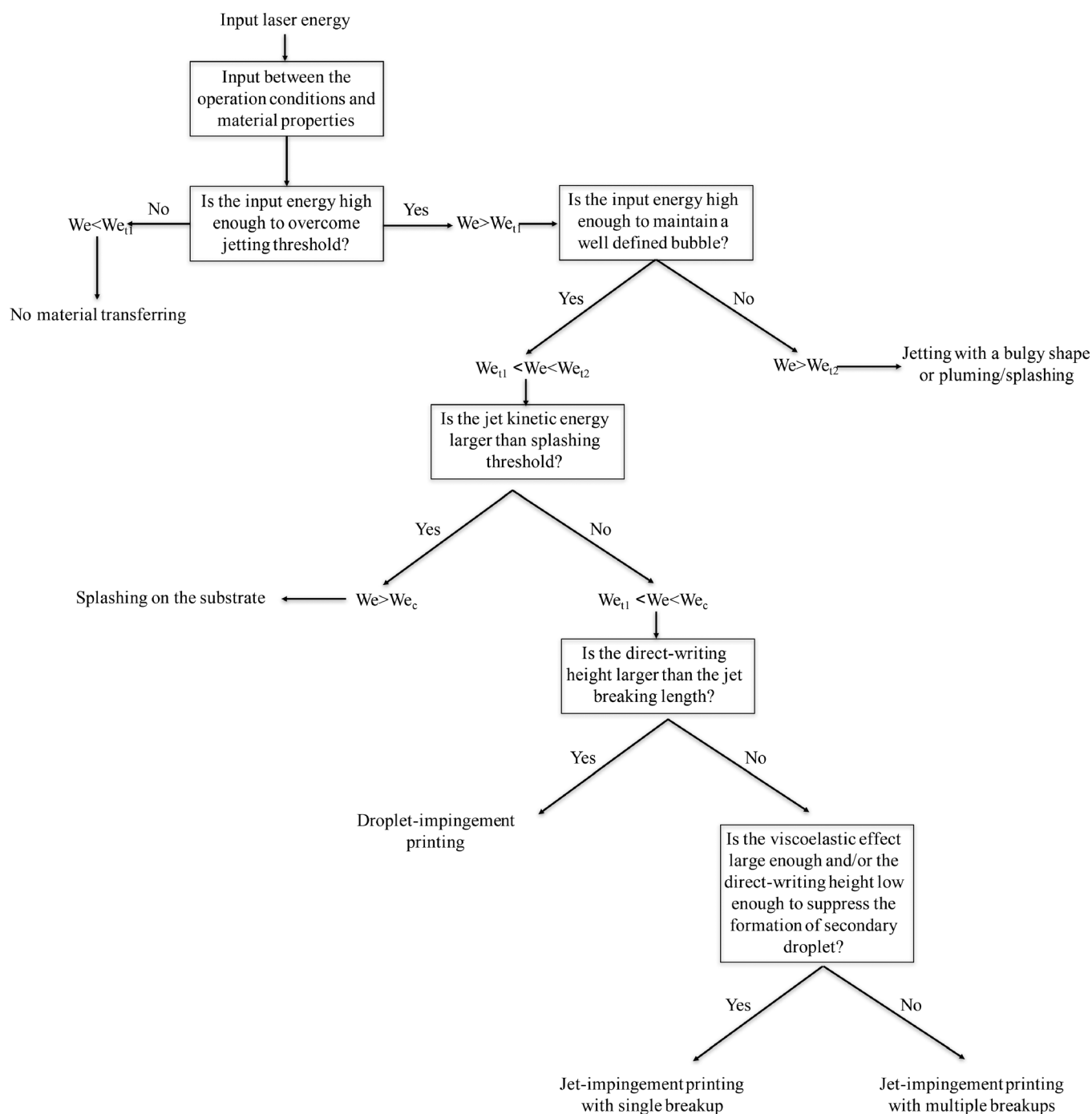


**FIG. 5.** Decision tree for printing type analysis. Adapted from Z. Zhang, R. Xiong, D. Corr, and Y. Huang, *Langmuir* **32**, 3004 (2016). Copyright 2016 American Chemical Society.

Every layer thickness has its own particular viscosity that the volume of the printed drop reaches its maximum and, at this stage, the specific viscosity is decreased at a lower thickness of the hydrogel. This effect was prominent as the height of the hydrogel layer was enlarged.<sup>107</sup>

Cell viability in laser bioprinting is related to factors such as laser energy, extracellular matrix film thickness, and the bioink viscosity.<sup>108</sup> On increasing the laser energy, the viability of cells may be reduced owing to the significant denaturation of DNA by ultraviolet light;



hence, an infrared laser may be preferred to ultraviolet lasers in the bioprinter framework. The respective cell viabilities can be considerably high if the laser energy conditions vary per thermal flux intensities. This phenomenon is correlated with the numerical models, indicating that (a) the thickness of the heated liquid water during the course of a laser pulse is only a few micrometers and (b) the complete cell droplet forms in a very short period of time (i.e., microseconds). The three different conditions causing mechanical stress in the laser-assisted cell printing could be the hydrodynamic pressure emerging from the bubble during its budding phase, the unfolding shear stress on the account of jet velocity during the jetting phase, and the conditions of landing that are consequent to the initial jet velocity and the thickness of the mattress.

Cells may withstand an initial compression accompanied by the inflation of the hydrodynamic pressure at the tip of the bubble where the formation of the singular point takes place; this does not have any pronounced effect on cell viability. Given the jet velocity = 50 m/s, the jet diameter = 10  $\mu\text{m}$ , the bioink density = 1.03 kg/l, and the viscosity equals 100 mPa s, the Reynolds number would approach zero. Despite reducing the viscosity and increasing the jet velocity, the Reynolds number still falls in the laminar flow regimen and should be 200. This figure is deduced to be less traumatizing for endothelial cells in comparison to the turbulent flow, which is an ephemeral occurrence. Moreover, increasing the bioink viscosity minimizes the jet velocity, thereby clearing away the secondary impact jet onto the glass substrate. Taken together, optimization of the laser energy, film thickness, and bioink viscosity is required to achieve viability of laser bioprinting of cells.<sup>108</sup>

## CONCLUSIONS

In recent years, the field of biofabrication in general and bioprinting, in particular, has witnessed advances owing to enthusiastic global attention from different fields such as engineering, medicine, and materials science. Although the technology has considerably matured, the underlying science of bioprinting is at times underappreciated. Herein, we have reviewed the basic physical principles that govern the bioprinting process for three of the most popular bioprinters: extrusion, inkjet, and laser-assisted bioprinters. Essential dominant parameters, as well as their relationship and governing equations, were described. This information can be used by both beginners and experts to optimize their bioprinting efforts. Acknowledgment of the science and formulas governing the bioprinting process may advance the field from the “trial and error” approach to the level of “prediction and control.”

## REFERENCES

- <sup>1</sup>L. Moroni, T. Boland, J. A. Burdick, C. De Maria, B. Derby, G. Forgacs, J. Groll, Q. Li, J. Malda, V. A. Mironov, C. Mota, M. Nakamura, W. Shu, S. Takeuchi, T. B. F. Woodfield, T. Xu, J. J. Yoo, and G. Vozzi, *Trends Biotechnol.* **36**, 384 (2018).
- <sup>2</sup>F. T. C. Moreira, R. A. F. Dutra, J. P. Noronha, and M. G. F. Sales, *Biosens. Bioelectron.* **56**, 217 (2014).
- <sup>3</sup>P. Mostafalu, W. Lenk, M. R. Dokmeci, B. Ziaie, A. Khademhosseini, and S. R. Sonkusale, *IEEE Trans. Biomed. Circuits Syst.* **9**, 670 (2015).
- <sup>4</sup>A. Shafiee, E. Ghadiri, J. Kassis, N. Pourhabibi Zarandi, and A. Atala, *Curr. Stem Cell Rep.* **4**, 105 (2018).
- <sup>5</sup>N. Genina, D. Fors, H. Vakili, P. Ihalainen, L. Pohjala, H. Ehlers, I. Kassamakov, E. Haeggstrom, P. Vuorela, J. Peltonen, and N. Sandler, *Eur. J. Pharm. Sci.* **47**, 615 (2012).
- <sup>6</sup>H.-W. Kang, S. J. Lee, I. K. Ko, C. Kengla, J. J. Yoo, and A. Atala, *Nat. Biotechnol.* **34**, 312 (2016).
- <sup>7</sup>S. G. Ju, M. K. Kim, C.-S. Hong, J. S. Kim, Y. Han, D. H. Choi, D. Shin, and S. B. Lee, *Radiat. Oncol. Biol.* **88**, 453 (2014).
- <sup>8</sup>E. Poulin, L. Gardi, A. Fenster, J. Pouliot, and L. Beaulieu, *Radiother. Oncol.* **114**, 335 (2015).
- <sup>9</sup>J. L. Silberstein, M. M. Maddox, P. Dorsey, A. Feibus, R. Thomas, and B. R. Lee, *Urology* **84**, 268 (2014).
- <sup>10</sup>N. N. Zein, I. A. Hanouneh, P. D. Bishop, M. Samaan, B. Eghtesad, C. Quintini, C. Miller, L. Yerian, and R. Klatte, *Liver Transplant.* **19**, 1304 (2013).
- <sup>11</sup>R. Olszewski, P. Szymor, and M. Kozakiewicz, *J. Cranio-Maxillofacial Surg.* **42**, 1847 (2014).
- <sup>12</sup>N. Adolphs, W. Liu, E. Keeve, and B. Hoffmeister, *Comput. Aided Surg.* **19**, 20 (2014).
- <sup>13</sup>Y. Sun, H.-T. Luebbes, J. O. Agbaje, S. Schepers, L. Vrielinck, I. Lambrechts, and C. Politis, *J. Craniofacial Surg.* **24**, 1871 (2013).
- <sup>14</sup>A. Shafiee and A. Atala, *Annu. Rev. Med.* **68**, 29 (2017).
- <sup>15</sup>C. Norotte, F. S. Marga, L. E. Niklason, and G. Forgacs, *Biomaterials* **30**, 5910 (2009).
- <sup>16</sup>B. Lorber, W.-K. Hsiao, I. M. Hutchings, and K. R. Martin, *Biofabrication* **6**, 015001 (2014).
- <sup>17</sup>R. Gaebel, N. Ma, J. Liu, J. Guan, L. Koch, C. Klopsch, M. Gruene, A. Toelk, W. Wang, P. Mark, F. Wang, B. Chichkov, W. Li, and G. Steinhoff, *Biomaterials* **32**, 9218 (2011).
- <sup>18</sup>Y. Nahmias, R. E. Schwartz, C. M. Verfaillie, and D. J. Odde, *Biotechnol. Bioeng.* **92**, 129 (2005).
- <sup>19</sup>A. Shafiee and A. Atala, *Trends Mol. Med.* **22**, 254 (2016).
- <sup>20</sup>V. Mironov, R. P. Visconti, V. Kasyanov, G. Forgacs, C. J. Drake, and R. R. Markwald, *Biomaterials* **30**, 2164 (2009).
- <sup>21</sup>P. Calvert, *Chem. Mater.* **13**, 3299 (2001).
- <sup>22</sup>R. D. Boehm, P. R. Miller, J. Daniels, S. Stafslie, and R. J. Narayan, *Mater. Today* **17**, 247 (2014).
- <sup>23</sup>P. Calvert and T. Boland, *Biopolymers and Cells Inkjet Technology for Digital Fabrication* (John Wiley & Sons, New York, 2014), pp. 275–305.
- <sup>24</sup>D. J. Odde and M. J. Renn, *Trends Biotechnol.* **17**, 385 (1999).
- <sup>25</sup>M. Ali, E. Pages, A. Ducom, A. Fontaine, and F. Guillemot, *Biofabrication* **6**, 045001 (2014).
- <sup>26</sup>A. Shafiee, C. Norotte, and E. Ghadiri, *Bioprinting* **8**, 13 (2017).
- <sup>27</sup>J. Groll, J. A. Burdick, D.-W. Cho, B. Derby, M. Gelinsky, S. C. Heilshorn, T. Jüngst, J. Malda, V. A. Mironov, K. Nakayama, A. Ovsianikov, W. Sun, S. Takeuchi, J. J. Yoo, and T. B. F. Woodfield, *Biofabrication* **11**, 013001 (2018).
- <sup>28</sup>N. Paxton, W. Smolan, T. Böck, F. Melchels, J. Groll, and T. Jungst, *Biofabrication* **9**, 044107 (2017).
- <sup>29</sup>L. Moldovan, C. M. Babbey, M. P. Murphy, and N. I. Moldovan, *Curr. Opinion Biomed. Eng.* **2**, 124 (2017).
- <sup>30</sup>D. E. Ingber, V. C. Mow, D. Butler, L. Niklason, J. Huard, J. Mao, I. Yannas, D. Kaplan, and G. Vunjak-Novakovic, *Tissue Eng.* **12**, 3265 (2006).
- <sup>31</sup>P. Lenas, M. Moos, Jr., and F. P. Luyten, *Tissue Eng., Part B* **15**, 381 (2009).
- <sup>32</sup>J. Basu and J. W. Ludlow, *Birth Defects Res., Part C* **96**, 30 (2012).
- <sup>33</sup>G. Forgacs and S. A. Newman, *Biological Physics of the Developing Embryo* (Cambridge University Press, 2005).
- <sup>34</sup>K. Jakab, C. Norotte, F. Marga, K. Murphy, G. Vunjak-Novakovic, and G. Forgacs, *Biofabrication* **2**, 022001 (2010).
- <sup>35</sup>K. Jakab, A. Neagu, V. Mironov, R. R. Markwald, and G. Forgacs, *Proc. Natl. Acad. Sci.* **101**, 2864 (2004).
- <sup>36</sup>K. Jakab, C. Norotte, B. Damon, F. Marga, A. Neagu, C. L. Besch-Williford, A. Kachurin, K. H. Church, H. Park, V. Mironov, R. Markwald, G. Vunjak-Novakovic, and G. Forgacs, *Tissue Eng., Part A* **14**, 413 (2008).
- <sup>37</sup>V. Mironov, T. Boland, T. Trusk, and G. Forgacs, *Trends Biotechnol.* **21**, 157 (2003).
- <sup>38</sup>N. I. Moldovan, N. Hibino, and K. Nakayama, *Tissue Eng., Part B* **23**, 237 (2017).
- <sup>39</sup>C. P. Heisenberg and Y. Bellaïche, *Cell* **153**, 948 (2013).
- <sup>40</sup>J. M. Pérez-Pomares and R. A. Foty, *Bioessays* **28**, 809 (2006).
- <sup>41</sup>M. S. Steinberg, *Science* **141**, 401 (1963).

- <sup>42</sup>F. Marga, K. Jakab, C. Khattiwala, B. Shepherd, S. Dorfman, B. Hubbard, S. Colbert, and G. Forgacs, *Biofabrication* **4**, 022001 (2012).
- <sup>43</sup>T. Lecuit and P.-F. Lenne, *Nat. Rev. Mol. Cell Biol.* **8**, 633 (2007).
- <sup>44</sup>B. S. Winters, S. R. Shepard, and R. A. Foty, *Int. J. Cancer* **114**, 371 (2005).
- <sup>45</sup>B. Hegedüs, F. Marga, K. Jakab, K. L. Sharpe-Timms, and G. Forgacs, *Biophys. J.* **91**, 2708 (2006).
- <sup>46</sup>M. S. Steinberg, *Symp. Soc. Exp. Biol.* **32**, 25 (1978).
- <sup>47</sup>M. S. Steinberg, *Integr. Biol.* **1**, 49 (1998).
- <sup>48</sup>R. A. Foty, G. Forgacs, C. M. Pflieger, and M. S. Steinberg, *Phys. Rev. Lett.* **72**, 2298 (1994).
- <sup>49</sup>R. A. Foty, C. M. Pflieger, G. Forgacs, and M. S. Steinberg, *Dev. Biol.* **122**, 1611 (1996).
- <sup>50</sup>C. Norotte, F. Marga, A. Neagu, I. Kosztin, and G. Forgacs, *Europhys. Lett.* **81**, 46003 (2008).
- <sup>51</sup>D. Duguay, R. A. Foty, and M. S. Steinberg, *Dev. Biol.* **253**, 309 (2003).
- <sup>52</sup>R. A. Foty and M. S. Steinberg, *Dev. Biol.* **278**, 255 (2005).
- <sup>53</sup>B. J. Damon, N. V. Mezentsseva, J. S. Kumaratilake, G. Forgacs, and S. A. Newman, *Dev. Biol.* **321**, 319 (2008).
- <sup>54</sup>G. Forgacs, R. A. Foty, Y. Shafir, and M. S. Steinberg, *Biophys. J.* **74**, 2227 (1998).
- <sup>55</sup>D. A. Beysens, G. Forgacs, and J. A. Glazier, *Proc. Nat. Acad. Sci.* **97**, 9467 (2000).
- <sup>56</sup>G. Forgacs and R. A. Foty, in *Function and Regulation of Cellular Systems: Experiments and Models*, edited by A. Deutsch, M. Falk, and W. Zimmerman (Birkhauser, Basel, 2004), pp. 269–277.
- <sup>57</sup>I. Kosztin, G. Vunjak-Novakovic, and G. Forgacs, *Rev. Mod. Phys.* **84**, 1791 (2012).
- <sup>58</sup>M. McCune, A. Shafiee, G. Forgacs, and I. Kosztin, *Soft Matter* **10**, 1790 (2014).
- <sup>59</sup>A. Shafiee, M. McCune, G. Forgacs, and I. Kosztin, *Biofabrication* **7**, 045005 (2015).
- <sup>60</sup>A. Shafiee, E. Ghadiri, D. Williams, and A. Atala, *Bioprinting* **14**, e00047 (2019).
- <sup>61</sup>M. L. Manning, R. A. Foty, M. S. Steinberg, and E.-M. Schoetz, *Proc. Nat. Acad. Sci.* **107**, 12517 (2010).
- <sup>62</sup>Y. He, F. Yang, H. Zhao, Q. Gao, B. Xia, and J. Fu, *Sci. Rep.* **6**, 29977 (2016).
- <sup>63</sup>J. E. Trachtenberg, P. M. Mountziaris, J. S. Miller, M. Wettergreen, F. K. Kasper, and A. G. Mikos, *J. Biomed. Mater. Res.* **102**, 4326 (2014).
- <sup>64</sup>L. Ouyang, C. B. Highley, C. B. Rodell, W. Sun, and J. A. Burdick, *ACS Biomater. Sci. Eng.* **2**, 1743 (2016).
- <sup>65</sup>L. Ouyang, R. Yao, Y. Zhao, and W. Sun, *Biofabrication* **8**, 035020 (2016).
- <sup>66</sup>A. Blaeser, D. F. Duarte Campos, U. Puster, W. Richtering, M. M. Stevens, and H. Fischer, *Adv. Healthcare Mater.* **5**, 326 (2016).
- <sup>67</sup>R. Suntornnond, E. Tan, J. An, and C. Chua, *Materials* **9**, 756 (2016).
- <sup>68</sup>H. Liu, Y. Li, and D. Li, *Int. J. Adv. Manuf. Technol.* **83**, 2039 (2016).
- <sup>69</sup>V. H. M. Mouser, F. P. W. Melchels, J. Visser, W. J. A. Dhert, D. Gawlitta, and J. Malda, *Biofabrication* **8**, 035003 (2016).
- <sup>70</sup>W. Liu, M. A. Heinrich, Y. Zhou, A. Akpek, N. Hu, X. Liu, X. Guan, Z. Zhong, X. Jin, A. Khademhosseini, and Y. S. Zhang, *Adv. Healthcare Mater.* **6**, 1601451 (2017).
- <sup>71</sup>T. Gao, G. J. Gillispie, J. S. Copus, P. R. A. Kumar, Y.-J. Seol, A. Atala, J. J. Yoo, and S. J. Lee, *Biofabrication* **10**(3), 034106 (2018).
- <sup>72</sup>K. Nair, M. Gandhi, S. Khalil, K. C. Yan, M. Marcolongo, K. Barbee, and W. Sun, *Biotechnol. J.* **4**, 1168 (2009).
- <sup>73</sup>W. Z. Samad, M. M. Salleh, A. Shafiee, and M. A. Yarmo, *AIP Conf. Proc.* **1284**, 83–86 (2010).
- <sup>74</sup>T. Kawase, T. Shimoda, C. Newsome, H. Sirringhaus, and R. H. Friend, *Thin Solid Films* **438–439**, 279 (2003).
- <sup>75</sup>W. Z. Samad, M. M. Salleh, A. Shafiee, and M. A. Yarmo, in *IEEE International Conference on Semiconductor Electronics (ICSE)* (2010).
- <sup>76</sup>F. C. Krebs, *Sol. Energy Mater. Sol. Cells* **93**, 394 (2009).
- <sup>77</sup>A. Shafiee, M. M. Salleh, and M. Yahaya, in *IEEE International Conference on Semiconductor Electronics, ICSE* (2008), pp. 319–322.
- <sup>78</sup>W. Z. Samad, M. M. Salleh, A. Shafiee, and M. A. Yarmo, *Mater. Sci. Forum* **663–665**, 694 (2010).
- <sup>79</sup>T. Boland, T. Xu, B. Damon, and X. Cui, *Biotechnol. J.* **1**, 910 (2006).
- <sup>80</sup>P. Calvert, *Science* **318**, 208 (2007).
- <sup>81</sup>F. Xu, S. J. Moon, A. E. Emre, E. S. Turali, Y. S. Song, S. A. Hacking, J. Nagatomi, and U. Demirci, *Biofabrication* **2**, 014105 (2010).
- <sup>82</sup>R. Rioboo, M. Marengo, and C. Tropea, *Exp. Fluids* **33**, 112 (2002).
- <sup>83</sup>R. Rioboo, C. Tropea, and M. Marengo, *Atomization Sprays* **11**, 12 (2001).
- <sup>84</sup>B. Derby, *Annu. Rev. Mater. Res.* **40**, 395 (2010).
- <sup>85</sup>D. Williams, *Essential Biomaterials Science* (Cambridge University Press, 2014).
- <sup>86</sup>J. N. Israelachvili, *Intermolecular and Surface Forces*, 3rd ed. (Academic Press, Amsterdam, 2011).
- <sup>87</sup>A. Shafiee, E. Ghadiri, M. Mat Salleh, M. Yahya, and A. Atala, *IEEE J. Electron Devices Soc.* (published online 2019).
- <sup>88</sup>N. Reis, C. Ainsley, and B. Derby, *J. Appl. Phys.* **97**, 094903 (2005).
- <sup>89</sup>M. H. Tsai, W. S. Hwang, H. H. Chou, and P. H. Hsieh, *Nanotechnology* **19**, 335304 (2008).
- <sup>90</sup>A. Shafiee, M. Mat Salleh, and M. Yahaya, *Proc. SPIE* **7493**, 74932D (2009).
- <sup>91</sup>S. Jung, Ph.D. thesis, University of Cambridge, Cambridge UK, 2011.
- <sup>92</sup>S. Schiaffino and A. Sonin, *Phys. Fluids* **9**, 3172 (1997).
- <sup>93</sup>G. D. Martin, S. D. Hoath, and I. M. Hutchings, *J. Phys.: Conf. Ser.* **105**, 012001 (2008).
- <sup>94</sup>W. Wang, Y. Huang, M. Grujicic, and D. B. Chrisey, *J. Manuf. Sci. Eng.* **130**, 021012 (2008).
- <sup>95</sup>P. Sopena, S. González-Torres, J. M. Fernández-Pradas, and P. Serra, *Sci. Rep.* **8**, 7999 (2018).
- <sup>96</sup>Y. Deng, P. Renaud, Z. Guo, Z. Huang, and Y. Chen, *J. Biol. Eng.* **11**, 2 (2017).
- <sup>97</sup>C. Mézel, A. Souquet, L. Hallo, and F. Guillemot, *Biofabrication* **2**, 014103 (2010).
- <sup>98</sup>F. Kaweck, W. P. Clafshenkel, F. A. Auger, J.-M. Bourget, J. Fradette, and R. Devillard, *Biofabrication* **10**, 035006 (2018).
- <sup>99</sup>N. T. Kattamis, M. S. Brown, and C. B. Arnold, *J. Mater. Res.* **26**, 2438 (2011).
- <sup>100</sup>A. Sorkio, L. Koch, L. Koivusalo, A. Deiwick, S. Miettinen, B. Chichkov, and H. Skottman, *Biomaterials* **171**, 57 (2018).
- <sup>101</sup>Z. Zhang, C. Xu, R. Xiong, D. B. Chrisey, and Y. Huang, *Biomicrofluidics* **11**, 034120 (2017).
- <sup>102</sup>Z. Zhang, R. Xiong, D. Corr, and Y. Huang, *Langmuir* **32**, 3004 (2016).
- <sup>103</sup>Z. Zhang, R. Xiong, R. Mei, Y. Huang, and D. B. Chrisey, *Langmuir* **31**, 6447 (2015).
- <sup>104</sup>L. Koch, O. Brandt, A. Deiwick, and B. Chichkov, *Int. J. Bioprint.* **3**, 42 (2017).
- <sup>105</sup>H. Desrus, B. Chassagne, F. Moizan, R. Devillard, S. Petit, R. Kling, and S. Catros, *Appl. Opt.* **55**, 3879 (2016).
- <sup>106</sup>S. Petit, O. Kérouédan, R. Devillard, and E. Cormier, *Appl. Opt.* **56**, 8648 (2017).
- <sup>107</sup>M. Gruene, C. Unger, L. Koch, A. Deiwick, and B. Chichkov, *Biomed. Eng. Online* **10**, 19 (2011).
- <sup>108</sup>S. Catros, B. Guillotin, M. Bačáková, J.-C. Fricain, and F. Guillemot, *Appl. Surf. Sci.* **257**, 5142 (2011).